Effect of Temperature on Flow-Induced Crystallization of Isotactic Polypropylene

Macromolecules

pubs.acs.org/Macromolecules

Article

Effect of Temperature on Flow-Induced Crystallization of Isotactic Polypropylene: A Molecular-Dynamics Study

Nikolaos I. Sigalas,* Stan A. T. Van Kraaij, and Alexey V. Lyulin

Cite This: *Macromolecules* 2023, 56, 8417−8427

Read Online

ACCESS | Metrics & More | Article Recommendations | Supporting Information

ABSTRACT: Molecular-dynamics simulations are employed in order to study the flow-induced crystallization (FIC) of isotactic polypropylene from a supercooled state at different temperatures. The study found that FIC displayed the highest rate at a temperature range of T_{max} = 330−360 K. By applying the mean first passage time method, the pre-nucleation, nucleation, and growth stages were successfully identified. The pre-nucleation stage was thoroughly examined, and multiple phenomena were observed, including unexpected strain hardening in the vicinity of T_{max} and the formation of high ordering areas that acted as nuclei precursors with limited motion along the tensile direction. Additionally, a non-uniformly slowed segmental relaxation was noted, which suggested the existence of cooperative rearranging regions, the percolation of which could potentially explain the strain hardening effect. Furthermore, the size of the critical clusters at the nucleation point was independent of temperature. Finally, stable clusters grew and merged, resulting in the formation of a shish network.

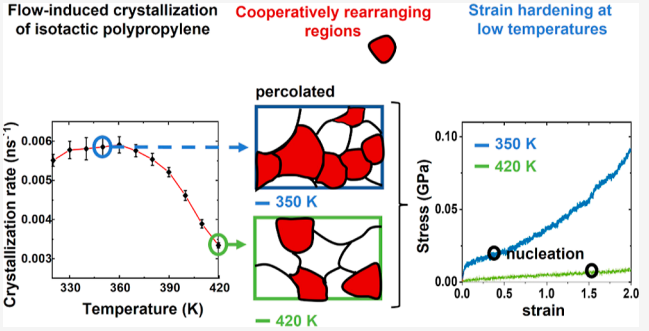

1. INTRODUCTION

Understanding flow-induced crystallization (FIC) of polyolefins is a crucial step in the development of more sustainable plastic packaging materials.[1] Currently, the films used in the food industry have rather high performance in terms of toughness, thermal resistance, and barrier properties.[2] However, large amounts of these films produced today cannot be recycled because of their multimaterial composition.[3] Commonly, metals and polymers of different chemical constitution are used in order to ensure good performance.[4] Thus, the development of environmentally more friendly "monomaterial packaging" solutions is highly desirable. "Monomaterial" here does not necessarily imply a single layer made of macromolecules of precisely the same chemical constitution and architecture, but rather a single or multiple layer(s) made of macromolecules of similar chemical constitution that may be recycled in a blended state.[5−7] The key element for tailoring monomaterial film properties is their morphology.

Morphology describes the size, shape, orientation, spatial arrangement, and connectivity of amorphous and crystalline regions spotted in semicrystalline films. By imposing flow, morphology and the macroscale properties of these materials can be altered significantly.[8] Commercially, flow is applied to cast or blown films using a carefully designed apparatus made by rolls, known as machine direction orientation (MDO).[9] During the MDO process, the semicrystalline film is heated to a temperature close to the melting temperature of the polymer, and then it is uniaxially stretched at a draw ratio close to 10, or even more in some cases.[10] Finally, the film is thermally treated in order to lock the new properties obtained from the stretching. This process has been proven to have a strong effect on the microstructure transformation from spherulitic to fibrillar and[11] enhances barrier properties[9] and tensile strength at break.[10] In the laboratory scale, it has been shown that by applying elongational flow with high strain rate to a supercooled melt at a temperature close to the melting point, not only morphology is affected, but kinetics as well, resulting in an increase of up to 6 orders of magnitude of the crystallization rate and in an ultrahigh performance.[12]

In addition to imposed flow, temperature can also affect the mobility of the chains, their orientation, and straightening. For instance, during the MDO process, the drawing stage is taking place at a temperature range above the α-relaxation temperature of the crystalline phase, where slip processes in the lamellae are activated.[13] Due to slipping, the lamellar crystals composing a spherulite can fragment and undergo a transformation to a shish-kebab structure.[14] Especially the size of the kebab structure heavily depends on the mobility of the chains and, thus, the temperature.[15] Additionally, flow at higher temperatures has a weaker effect on the elongation of the polymer chain than that at

Received: May 11, 2023
Revised: October 18, 2023
Accepted: October 23, 2023
Published: November 3, 2023

lower temperatures. Therefore, temperature can be crucial for the elongation of a supercooled polymer melt as well and subsequently for the nucleation and the final crystalline structure. Such an effect was reported by Okada et al.,[16] who showed that the emergence of nano-oriented crystals (NOCs) during FIC of isotactic polypropylene (iPP) is possible only within a specific temperature range (150−167 °C) close to the iPP equilibrium melting point (187 °C). So, the processing parameters can be crucial for the final performance of the polymer film.

In order to be able to tailor the final properties of the film, the intermediate stages of crystallization should be well-known. Normally, crystallization has been characterized as a multistep process.[17] As far back as in the late 1990s, density fluctuations prior to crystallization under quiescent conditions were reported,[18,19] while later research[20,21] showed evidence that a mesomorphic structure precedes the well-defined lamellar crystal. Even if the exact structure of the mesophase still remains an open question, progress has been made toward understanding the different stages of the formation of such precursor. More specifically, Li et al.[22] described four different stages during FIC of partially cross-linked iPP: conformation order, density fluctuation, orientation order, and crystal order. The sequence of the stages is not exact, and it seems that it depends on the processing conditions. For instance, it has been reported that, under low shearing conditions, conformation order comes first, followed by density fluctuation and orientation order, while under strong shearing, conformation order and orientation order take place at the same time.[23] The latter is supported further by An and colleagues[24,25] who reported that the iPP helical segments can stabilize and increase their lifetime synergistically by forming helical bundles.

In this work, a systematic molecular-dynamics study of FIC in iPP starting from a supercooled melt at different temperatures is presented. Focus is placed on the early stages of FIC prior to and slightly after nucleation. Kinetics of FIC are obtained using the mean first passage method, which has already been used for various systems, such as argon vapor,[26] *n*-eicosane,[27,28] and polyethylene.[29] Yamamoto[30] also studied the FIC of iPP, but for an unentangled polymer melt. In the present study, longer, entangled iPP melts have been considered, in order to mimic the polymer structure of experimental samples. A dynamic analysis of the polymer on different spatial scales is included as well.

The review is organized as follows. In Section 2, the models and the molecular-dynamics simulation details are described. In Section 3, results on the kinetics and structural and dynamical properties of iPP during FIC are presented at different temperatures. Finally, in Section 4, the conclusions of this study are drawn, and possible next steps are discussed.

2. MODEL AND SIMULATION DETAILS

2.1. Model and Simulation Process. Our goal was to study the effect of temperature on the FIC of iPP using molecular-dynamics simulations. For this purpose, an iPP melt of 20 chains of 2000 monomers per chain was simulated. An iPP monomer comprised a methyl group (CH_3), a methylene group (CH_2), and a methine group (CH) in the united atom representation where carbons and hydrogens are fused into one single united atom. We used the TraPPE-UA force field, that was initially developed by Martin and Siepmann[31] and then modified by Pütz et al.,[32] to describe all the bonded and nonbonded interactions between different groups. The intramolecular nonbonded interactions are calculated only for united atoms that are four or more bonds apart. It should be noted that charges are not taken into account. TraPPE-UA has been extensively used in crystallization studies of polymers with a focus on the interphase properties of semicrystalline iPP[33] and on the FIC of both polyethylene[34] and iPP.[30] Ranganathan et al.[35] have claimed that TraPPE-UA is promising for the investigation of semicrystalline polymers with diverse branching architecture as well. Comparing TraPPE-UA to other united atom force fields,[36] it has been proven that TraPPE-UA reproduces better thermodynamic properties like density and thermal expansion coefficient in the melt and in the glassy state.[37]

All the simulations were performed with Gromacs software package version 2020.3.[38] The first step was to create the initial configuration of the system with 100% isotacticity using the Materials and Process Simulations (MAPS) platform developed by Scienomics.[39] After that, the iPP melt was equilibrated at 500 K, above the melting temperature T_m of high molar mass iPP reported as 460 K.[40] The equilibration was completed in three different steps: (1) an energy minimization, using the steepest descent algorithm which converged when the maximum force was smaller than 10 kJ/(mol nm); (2) a simulation in the canonical ensemble (NVT), which lasted for 5 ns using the velocity rescaling thermostat with time constant $\tau(T) = 0.5$ ps; (3) a simulation in the NPT ensemble, which lasted for 1.5 μs using the Nosé−Hoover thermostat with time constant $\tau(T) = 0.5$ ps and the Parrinello−Rahman barostat[41] with time constant $\tau(P) = 5$ ps. After the equilibration, five different configurations were extracted from the trajectory produced at step three at not equidistant times (100.0, 230.0, 456.0, 601.5, and 750.5 ns). All the configurations had a characteristic ratio of $C_\infty = 6.4$, close to the computational value that was estimated for well relaxed single unperturbed iPP polymer chains using the TraPPE-UA force field.[42] The five configurations were cooled with a cooling rate of 1 K/ns to the desired temperature. In total, 40 equilibrated systems were studied at eight different temperatures from 350 to 420 K with step 10 K, five systems at each temperature. Finally, each iPP supercooled melt was submitted to a simulation in the $N\dot{e}_{xx}P_{yy}P_{zz}T$ ensemble with strain rate $\dot{e}_{xx} = 10^7\ s^{-1}$ and $P_{yy} = P_{zz} = 1$ bar, which lasted for 200 ns. All of the simulation boxes were stretched three times their initial lengths along the x axis. For all the simulations, a Verlet neighbor list for Lennard-Jones interactions was used with cutoff distance for short-range neighbor list $r_{list} = 1.4$ nm. In addition, a plain cutoff with an unmodified van der Waals potential was used with tail corrections for energy and pressure. The cutoff distance for van der Waals interactions was 1.2 nm.

2.2. Orientation Order Parameter along the Tensile Direction. In order to quantify the chain orientation, we focus on the orientation of local chord vectors along the tensile direction. Specifically, we created chord vectors connecting backbone united atoms that are six bonds apart. Then, the orientational order parameter along the tensile direction is calculated as a Legendre polynomial of second order

$$P_{2,x} = \left\langle \frac{3\cos^2\theta - 1}{2} \right\rangle \quad (1)$$

where θ is the angle between a chord vector and a unit vector along the tensile x direction. The $P_{2,x}$ is averaged over all chord vectors in the simulation box.

2.3. Helical Sequence Length. For the estimation of the length of the helices, what constitutes a helical segment must be defined. An iPP helical segment comprises five backbone atoms

https://doi.org/10.1021/acs.macromol.3c00916
Macromolecules 2023, 56, 8417−8427

and can be either left-handed (LH) or right-handed (RH). To define a helical segment, first of all, we calculate all the dihedral angles ϕ along the backbone of the chains according to IUPAC convention.[43] Then, we characterize the dihedral angles as *trans* ($180 \pm 30°$), *gauche*$^+$ ($-60 \pm 30°$), and *gauche*$^-$ ($+60 \pm 30°$). A segment that consists of five backbone atoms is characterized further as RH or LH, if a sequence of (*trans*)(*gauche*$^+$) or (*gauche*$^-$)(*trans*) is spotted, respectively. Finally, the weight-averaged value of the length $\langle l_h \rangle$[30] of these helical segments has been measured as

$$\langle l_h \rangle = \frac{\sum_{l_h} n(l_h) l_h^2}{\sum_{l_h} n(l_h) l_h} \quad (2)$$

where l_h is the length of some particular helical sequence and $n(l_h)$ is the number of helical sequences with length l_h.

2.4. Crystallinity. Crystallinity is measured according to Yamamoto.[30] Briefly, having defined a helical segment, we can calculate its position and direction. Then, two helical segments are considered parallel if:

(i) they form an angle less than 30°;
(ii) their distance along the tensile direction is less than $\frac{p}{2}$, where p is the pitch per monomer which is equal to one-third of the length of the helical repeat unit $p = \frac{0.65}{3}$nm;
(iii) their distance perpendicular to the tensile direction lies in between 1.4σ and 1.9σ, where $\sigma = 0.395$ nm is the distance at which the Lennard-Jones potential energy for CH_2 united atoms becomes zero.

Helical segments that have two or more neighbors are considered crystalline. Crystallinity χ_c is defined as the ratio of crystalline atoms over the total number of atoms. Moreover, if two crystalline segments are within a radial distance of 1.8σ, then they are considered to belong to the same cluster. In this way, the number and the size of clusters can be calculated.

2.5. Mean First Passage Time Method. A mean first passage time (MFPT) analysis can be applied to the largest cluster of the system n_{max} according to Yi et al.[29]

$$\tau(n_{max}) = 0.5\tau^*[1+\mathrm{erf}(Z\sqrt{\pi}(n_{max} - n^*))] + 0.5G^{-1}(n_{max} - n^*)[1+\mathrm{erf}(C(n_{max} - n^*))] \quad (3)$$

where MFPT $\tau(n_{max})$ is defined as the time at which a crystalline cluster of size n_{max} appears for the first time in the bulk, τ^* is the nucleation time, n^* is the critical nucleus size, G is the growth rate, Z is the so-called Zeldovich factor, which is the probability that a nucleus at the top of the barrier will stabilize instead of dissolving, and C is a constant chosen equal to a large positive value.[29]

MFPT is a method in which nucleation is perceived as an activation process with an energy nucleation barrier. There is a reaction coordinate that determines the state of the process, which is the cluster size in our case. The main assumptions for this method are[26]

1. The process is a steady-state process.
2. The energy barrier is relatively high.

The steady-state process is defined as a condition in which the net rate of growth of clusters of one size to the next larger size is the same for clusters of all sizes. In other words, the distribution of the cluster sizes for clusters smaller than the critical size will not change with time. This assumption holds also for the present study, for which the nucleation is homogeneous. On top of that, the simulation box is large enough for the small unstable clusters to grow independently before they reach their critical size. Moreover, the MFPT with respect to the reaction coordinate, i.e., the cluster size, exhibits a sigmoidal shape. The plateau value of this graph is related to the critical nucleation time. In order to accurately extract this time, the nucleation and growth must be distinct over time, meaning that the nucleation barrier should be high. In cases that the nucleation is not the rate limiting step, the nucleation time still can be extracted as it was showed by Wedekind et al.,[26] but care should be taken on the estimation of the rates. Yi et al.[29] recently tried to tackle this problem by adding an extra term to account for finite crystal growth rate, when the condition of the high energy barrier is not applied. The latter extension is given in eq 3. Overall, the MFPT is a well-defined method and it is usually preferred over other methods as discussed by Chkonia et al.[44] and it has been extensively used for different systems under both quiescent and flow conditions.[23,45]

2.6. Pre-nucleation Stages. In order to capture the behavior of the system at the pre-nucleation stages, we distinguish the united atoms in two classes, "nucleating" and "melting" atoms. Specifically, we choose a configuration of the system after the nucleation time at the so-called classification time t_c and the atoms that are crystalline and belong to a crystalline cluster are tagged as "nucleating", while the rest of the atoms in the amorphous phase are tagged as "melting". Then, we go backward in time and keep these specific tags for each atom. In this way, we can spot from $t = 0$ ns up to $t = t_c$, which atoms are going to nucleate.

Having classified the atoms, we measured the orientational order parameter along the x axis of both the "nucleating" and "melting" groups. For each atom, we calculate a local order parameter $P_{2,x(\mathrm{local})}$ defined as the average order parameter $P_{2,x}$ (eq 1) of all of the chord vectors within a radial distance $r_{OP} = 1.6\sigma$ from the center of each atom. Finally, we average the local $P_{2,x(\mathrm{local})}$ for all of the "nucleating" and all of the "melting" atoms, separately. The same procedure is used for the orientational order parameters along the y and z axis, $P_{2,y(\mathrm{local})}$ and $P_{2,z(\mathrm{local})}$, respectively.

3. RESULTS AND DISCUSSION

3.1. Equilibration. The iPP box of 20 chains of 2000 monomers per chain was equilibrated at 500 K, a temperature above the experimental melting point for high molar mass iPP at 460 K,[40] for a simulation time of 1500 ns. The method used for generating the initial structure, following the work of Theodorou and Suter,[39] and the subsequent three step equilibration process described in Section 2, resulted in an iPP conformation representative of a melt with an average characteristic ratio $C_\infty = 6.0 \pm 0.4$, measured in equilibrium conditions. Experimental $C_\infty = 6.2$[46] and simulation $C_\infty = 6.4$[42] values are in good agreement. The simulated melt is highly entangled with entanglement molecular weight $M_e = 3092$ g/mol (74 monomers per entanglement), which was estimated by using the CReTA (Contour Reduction Topological Analysis) algorithm.[47] Eckstein et al. calculated the entanglement molecular weight for iPP $M_e = 5100-5500$ g/mol[48] (121−130 monomers per entanglement). The underestimated value of M_e in the present study in comparison to the experimental value can lead to a higher stress localization, although it still has a reasonable value. Additionally, the density was measured as $764\frac{\mathrm{kg}}{\mathrm{m}^3}$, in good agreement with experimental results $\left(710 - 764\ \frac{\mathrm{kg}}{\mathrm{m}^3}\right)$.[49]

https://doi.org/10.1021/acs.macromol.3c00916
Macromolecules 2023, 56, 8417−8427

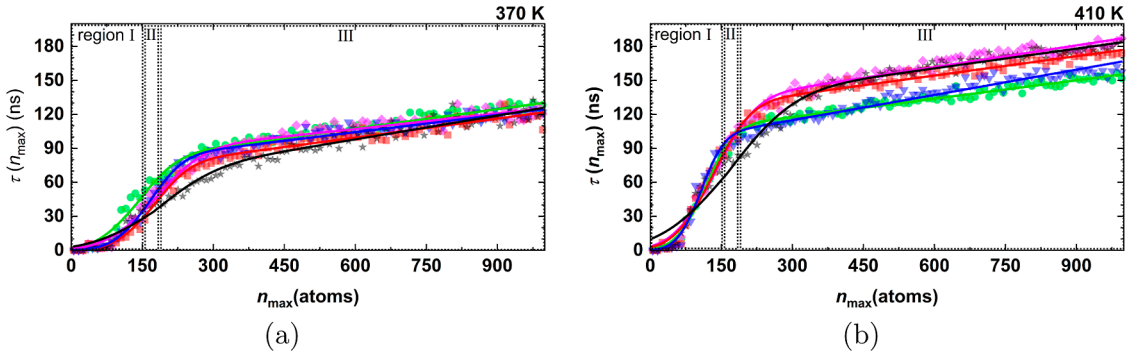

Figure 1. MFPT $\tau(n_{max})$ is plotted against the cluster size n_{max} for two different temperatures (a) 370 and (b) 410 K. In each panel, the different colored symbols [circle (green), rhombus (pink), square (red), triangle (blue), and asterisk (black)] represent simulations starting from a different initial configuration in the ensemble $Ne_{xx}P_{yy}P_{zz}T$ at equal strain rate and temperature. The data points are fitted with solid lines using eq 3 from Section 2.5. Both graphs are divided in three regions marked by dotted frames: (I) pre-nucleation (II) nucleation (III) growth.

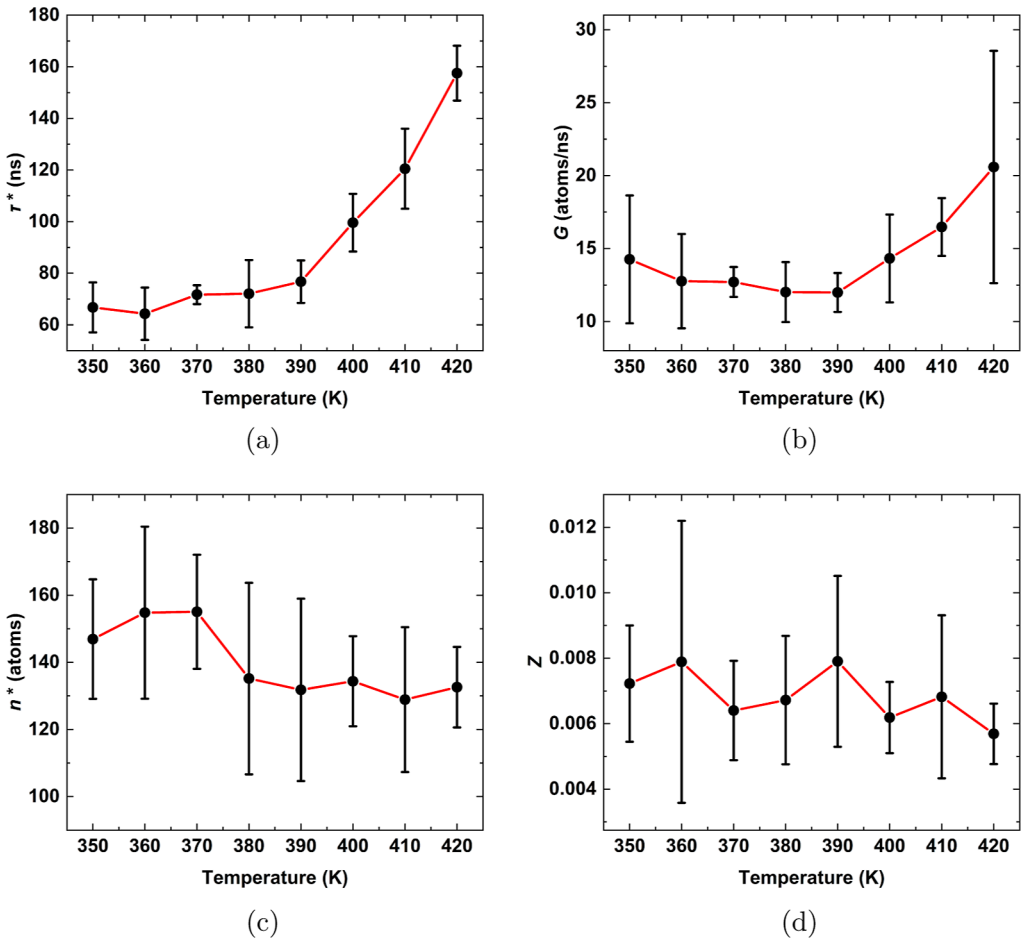

Figure 2. Temperature dependence of (a) nucleation time τ^*, (b) growth rate G, (c) critical nucleus size n^*, and (d) Zeldovich parameter Z which were extracted using eq 3. For all the variables at each temperature, a mean value is averaged over five simulations and is plotted together with its standard deviation.

After the equilibration was completed, five different configurations were extracted from the whole trajectory. Each configuration was further cooled and uniaxially stretched up to strain $\epsilon = 2$ at temperatures ranging from 350 to 420 K, as described in Section 2, above the glass transition temperature T_g = 305.6 K estimated with a cooling rate equal to 0.1 K/ns (see Supporting Information). The divergence of the estimated glass-transition temperature from the experimental value T_g = 272 K[50] can be attributed to the ultrafast cooling rates used in simulations. All of the properties that are calculated below have been averaged over five different simulations at each temperature. For the favor of the furthering discussion, the temperatures are divided into three categories: low (350−370 K), medium (380−390 K), and high temperatures (400−420 K). We should stress that our simulations probe a wide temperature range, above the glass transition temperature and below the melting temperature, where the crystallization rate is expected to exhibit a maximum. Especially temperatures close to

https://doi.org/10.1021/acs.macromol.3c00916
Macromolecules 2023, 56, 8417−8427

the glass transition temperature are not easily accessible experimentally for studying FIC given that iPP crystallizes upon cooling way before flow has any effect.[51] Previous studies on the FIC of iPP focused at temperatures from 423 to 440 K.[16]

3.2. Kinetics of iPP Crystallization. In order to study the kinetics of FIC, the MFPT method was used.[29,44] In essence, for each simulation run, the MFPT $\tau(n_{max})$ was recorded when a cluster of a specific size n_{max} emerged for the first time. The uniaxial stretching simulations of the present study lasted in total 200 ns, and the coordinates of the united atoms were recorded every 50 ps. Then, the cluster sizes were divided into small bins of 10 atoms. In each bin, the MFPT was averaged out. In Figure 1, the MFPT $\tau(n_{max})$ is plotted vs n_{max} at two temperatures 370 and 410 K. For each temperature, the data from five different simulations are plotted and fitted by eq 3. In Figure 1a,b, three different regions can be distinguished: (I) pre-nucleation, (II) nucleation, and (III) growth. During the pre-nucleation stage, small unstable clusters start to emerge. Some of the small clusters reach the size of the critical nucleus, and either they surpass it and nucleate or dissolve into the melt. At the nucleation point, the clusters have increased up to the size of a stable nucleus. This step is a critical step for crystallization after which the growth of crystal starts. During growth, amorphous chain segments from the surrounding melt are incorporated in the crystal phase. The growth rate and the final size of crystals depend on various parameters. In this study, the temperature dependence of the nucleation time τ^*, growth rate G, size of critical nucleus n^*, and Zeldovich parameter Z were investigated. We summarize the main findings below:

- The relationship between nucleation time τ^* and temperature exhibits a different trend below and above 390 K (Figure 2a). Below 390 K, τ^* remains relatively constant, with a range from 60 to 80 ns. However, above 390 K, τ^* increases much faster to values up to 160 ns at 420 K. This reflects the fact that nucleation becomes more difficult when supercooling is decreased. The observed temperature dependence of τ^* is also consistent with experimental observations on iPP under quiescent conditions,[52] with the transition temperature occurring at 390 K, above which the nucleation time begins to increase significantly.

- Both previous experimental[53] and some simulation studies[54] have shown that the growth rate G of the crystallized polymeric material exhibits a bell-shaped dependence on temperature with a maximum value observed below the melting point. However, in our simulations, no such maximum value was clearly observed (see Figure 2b) within the temperature range of 350−420 K. Instead, G increased with temperature above 390 K, while below 390 K, G exhibited variations without any abrupt changes. A maximum could be possibly observed if we would study temperatures closer to the melting point. The melting point of oriented melt is estimated to be approximately 50 K above[55] the melting point of the isotropic melt of iPP T_m = 460 K.[40] The studied temperature range in the current simulations, 350−420 K, is far away from the melting point of FIC around 510 K. It should be taken into account, however, that at the highest temperature, T = 420 K, nucleation could be barely observed within a simulation of 200 ns when the sample had already been stretched to strain ϵ = 2. Study of temperatures closer to the melting point would require much larger systems and larger ϵ.
- Both critical nucleus size n^* and Zeldovich parameter Z exhibit a weak temperature dependence. Specifically, n^* ranges from 120 to 160 atoms, with an average value of 140 atoms across all temperatures. Meanwhile, Z hovers around 0.007, which suggests that approximately 0.7% of the precursor clusters will become stable nuclei.

3.3. Dynamics of Supercooled iPP Melts. By analysis of the kinetics of FIC, nucleation events and growth could be clearly distinguished at different temperatures. It has been shown that, by imposing flow, the nucleation time τ^* is increased by many orders of magnitude in comparison to quiescent conditions.[12,52] It should be noted, however, that the strain rate $\dot{\epsilon}_{xx}$ used in this study is very high in comparison to experiments and τ^* can be affected by $\dot{\epsilon}_{xx}$. It has been proven that $\dot{\epsilon}_{xx}$ of the order of few s^{-1} has barely any effect on the crystallization of iPP,[12] while for the ultra fast $\dot{\epsilon}_{xx}$, iPP can exhibit a glassy behavior. It is important to verify whether some polymer segments do relax within the simulation deformation time and on which scale.

For this reason, we studied the polymer relaxation for supercooled iPP polymer melts before any further crystallization analysis. We performed an *NPT* simulation for 100 ns for the same iPP system that it was described in Section 2, at temperature range from 350 to 420 K. The focus is paid on chain and segmental dynamics that were estimated through the reorientation of the polymer chain end-to-end vectors and Kuhn segments, respectively, while results on the displacement of the united atoms are presented as well. The polymer chain end-to-end vector connects the first and the last united atom of a chain, while a Kuhn segment comprises 4 monomers. The reorientation was quantified using the second order Legendre autocorrelation function

$$\mathrm{ACF}_{P_2}(t) = \frac{1}{2}[3\langle(\mathbf{b}(0)\cdot\mathbf{b}(t))^2\rangle - 1] \tag{4}$$

where $\mathbf{b}$ is the unit vector along either an end-to-end vector or a vector connecting backbone atoms that are eight bonds apart (4 monomers). The autocorrelation functions were fit by a stretched exponential Kohlrausch−Williams−Watts (KWW) function[56]

$$P_{KWW}(t) = (1 - a)\exp\left[-\left(\frac{t}{\tau_{KWW}}\right)^{\beta}\right] \tag{5}$$

where a is the amplitude of the initial fast exponential decay, τ_{KWW} is the characteristic relaxation time, and β is the stretching exponent. The relaxation time τ_{KWW} of the end-to-end vectors exceeds 30 μs for all the temperatures from 350 to 420 K, being significantly slower in comparison to the $\tau_d = \frac{1}{\dot{\epsilon}_{xx}}$=100 ns. This indicates that certainly within this temperature range, chains as a whole do not relax within the reported τ_d and viscous flow of the material is suppressed. The polymer exhibits either an elastic or a glassy behavior in the temperature range 350−420 K and this is determined by the local relaxation of the Kuhn segments and the united atoms which is fast enough in order to affect the behavior of the material. The average relaxation time of the Kuhn segments τ_{Kuhn}, which is calculated using eqs 4 and 5, is found to be in the scale of 1 ns at high temperatures (400−420 K), significantly smaller than τ_d. At medium (380−390 K) and low temperatures (350−370 K), τ_{Kuhn} increases by 1−2 orders of

https://doi.org/10.1021/acs.macromol.3c00916
Macromolecules 2023, 56, 8417−8427

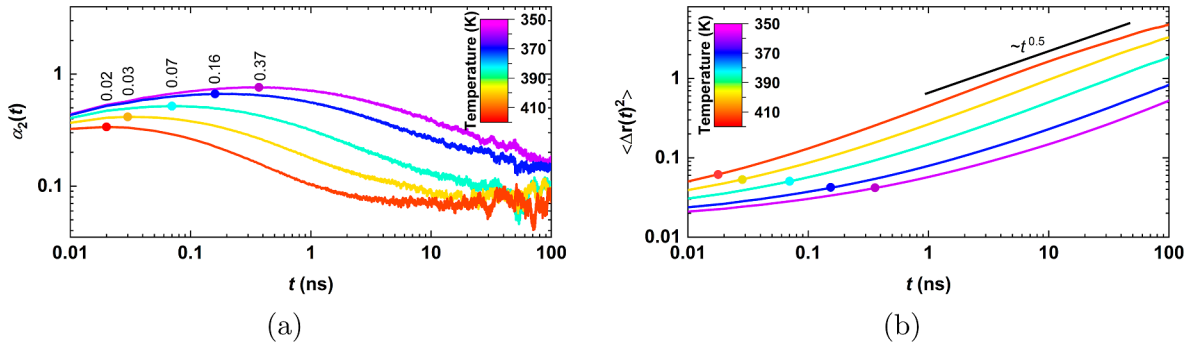

Figure 3. Time evolution of (a) non-gaussian parameter $\alpha_2(t)$ and (b) mean square displacement $\langle \Delta \boldsymbol{r}(t)^2 \rangle$ calculated for all the united atoms in the simulation box for temperatures ranging from 350 to 420 K. The colored dots indicate the caging time which was calculated from the time at which $\alpha_2(t)$ peaks.

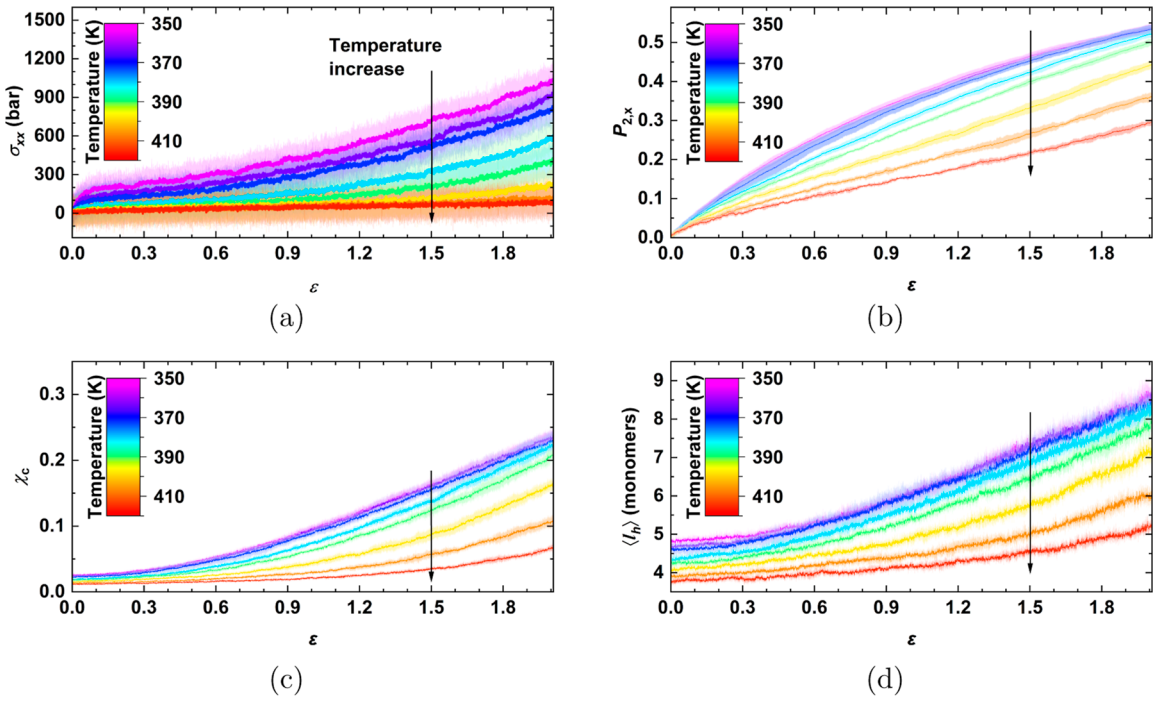

Figure 4. (a) Stress σ_{xx} along the tensile direction, (b) orientational order parameter $P_{2,x}$ along the tensile direction, (c) Crystallinity χ_c, and (d) average helical sequence length $\langle l_h \rangle$ plotted vs the engineering strain ϵ. The simulation lasted 200 ns. All the variables are averaged out of five simulations and are plotted at different temperatures from 350 (violet) to 420 K (red) as solid lines together with their standard deviation. The arrow points toward the direction of the temperature increase.

magnitude, respectively, and becomes comparable to τ_d. The relaxation of the individual Kuhn segments displays a nonuniform behavior throughout the entire polymer supercooled liquid, and this behavior is more pronounced at low temperatures (see Supporting Information). A further quantification of the heterogeneous local dynamic behavior is the estimation of the non-gaussian parameter $\alpha_2(t)$ of the individual united atoms. In the case that the distribution of the individual united atom displacements diverge from a Gaussian shape, $\alpha_2(t)$ is nonzero and peaks at the time which signifies the transition from the cage to the subdiffusive regime of the mean squared displacement $\langle \Delta \boldsymbol{r}(t)^2 \rangle$.[57,58] Thus, $\alpha_2(t)$ and $\langle \Delta \boldsymbol{r}(t)^2 \rangle$ were also calculated for the supercooled iPP polymer melts at temperatures ranging from 350 to 420 K and their time dependence is depicted in Figure 3a,b, respectively. The colored dots correspond to the caging time, which was estimated as the time when $\alpha_2(t)$ peaks. It can be seen in Figure 3a that the caging time increases upon decreasing the temperature from 420 to 350 K, approximately 1 order of magnitude, from 0.02 to 0.37 ns, respectively. In Figure 3b, the purple curve which corresponds to the lowest temperature equal to 350 K has two distinct regions: the caging region from 0.01 to 0.37 ns and the subdiffusive region from 10 to 100 ns. From 0.37 to 10 ns, the transition between the two regions takes place: change in slope. In the subdiffusive region, $\langle \Delta \boldsymbol{r}(t)^2 \rangle$ scales with time as $\sim t^{0.5}$. As temperature increases, the two regions are becoming less distinct.

The emergence of this dynamic heterogeneity can be explained by the fact that the structural relaxation takes place in collectively rearranging regions (CRRs) that strongly diverge in size.[59] The existence of CRRs does not necessarily imply that the polymer is in the glassy regime. As was shown, the deformation time τ_d exceeds the caging time and becomes comparable to the average relaxation time of Kuhn segments τ_{Kuhn} at low temperatures. Glassy behavior arises when the local relaxation of the individual units, i.e., Kuhn segments or smaller units, is significantly larger than the deformation time τ_d. So, we

https://doi.org/10.1021/acs.macromol.3c00916
Macromolecules 2023, 56, 8417−8427

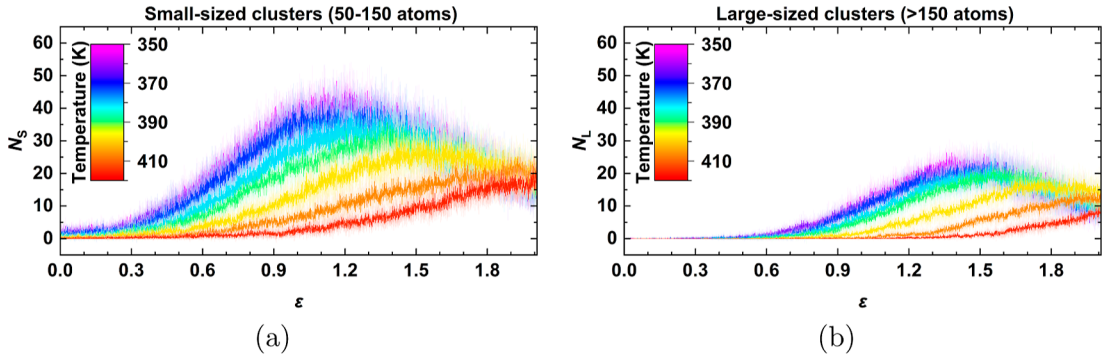

Figure 5. Cluster number of (a) small-sized clusters N_S and (b) large-sized clusters N_L plotted against the engineering strain rate ϵ. The simulation lasted for 200 ns. The small-sized clusters range from 50 to 150 atoms, while the large-sized clusters comprise more than 150 atoms. N_S and N_L are plotted at different temperatures from 350 K (violet) to 420 K (red) as solid lines together with their standard deviation. Each solid line was extracted by averaging five different simulations at each temperature.

can assume that iPP is in the rubbery regime. The fact that different local domains exhibit different dynamic behavior can still affect the mechanical response and the nucleation, as is discussed in Section 3.7.

3.4. Mechanical and Structural Characteristics of FIC.

Next we describe the results of mechanical response, orientation, crystallinity, growth of helices, and cluster number. In Figure 4a, the stress along the tensile direction σ_{xx} is plotted against the engineering strain ϵ at different temperatures. Initially, the elastic response, $\sigma \sim \epsilon$, can be spotted within 2% of deformation. It is less prominent at high temperatures. The elastic response can be attributed to the hard degrees of freedom of the polymer small backbone segments rotation (e.g., bonds, Kuhn segments), bending, torsional movement, etc. Young's modulus E was also measured in the linear elastic region. At low temperatures, E ranges from 0.2 to 0.4 MPa, and then it decreases to 0.1 MPa at medium temperatures and drops below 0.05 MPa at high temperatures. Experimental data have shown that E for rubber typically ranges from 0.01 to 0.1 MPa. So, as temperature increases, the polymer behaves more as a soft rubber. At the yield point, stress relaxation is observed due to segmental rotation. After the stress has relaxed for some time, strain hardening is observed only for low and medium temperatures. Especially for low temperatures, the strain hardening takes places way before the nucleation point, while at medium temperatures, it starts close or even after the nucleation point. At high temperatures, even if nucleation has occurred, stress exhibits a rather linear behavior.

The alignment of the polymer chains along the tensile direction is clearly visible, as shown in Figure 4b. The orientation of the chains was measured locally, as described in Section 2. At low temperatures, $P_{2,x}$ increases considerably during the pre-nucleation stage. It should be noted that the slope of the curve is constantly decreasing, revealing that orientation of the chains becomes more difficult with the increase of strain. The final value of $P_{2,x}$ is close to 0.5 for low temperatures, indicating that the polymer is aligned along the tensile direction, while at high temperatures, $P_{2,x}$ drops below 0.3.

Additionally, the crystallinity χ_c is plotted in Figure 4c. It can be seen that there is a lag time for all of the temperatures before χ_c starts to increase, while it increases considerably only after the nucleation time. It should be noted that the method we are using slightly overestimates χ_c, which is above zero at zero strain, contrary to what was expected given that the polymer is in a supercooled amorphous state. Moreover, at medium and high temperatures, a rise in temperature leads to a lower χ_c. At low temperatures, the curves overlap, indicating that the effect of temperature is negligible.

The average helical sequence length $\langle l_h \rangle$ develops similarly to χ_c; see Figure 4d. At zero strain and low temperatures, supercooled melts are richer in lengthier helices than the supercooled melts at high temperatures. At small strains below 0.3, there is no change in the length of helices regardless the temperature. Only after some time does $\langle l_h \rangle$ increase with strain before nucleation.

Besides, in order to gain some insights into the morphology of iPP upon FIC, a cluster analysis is performed. Upon crystallization, clusters of different sizes were developed and we distinguished the clusters in two different categories: small-sized clusters (50−150 atoms) and large-sized clusters (>150 atoms). Clusters below 50 atoms are too small, and they are not taken into account. As shown in Section 3.2, the critical size of the clusters for all of the temperatures fluctuates around 120−160 atoms. So, it is safe to assume that clusters below 150 are considered unstable and that is why they are tagged as small-sized. In Figure 5a,b, the number of small-sized clusters N_S and the number of large-sized clusters N_L are plotted, respectively. Overall, when N_S increases during the pre-nucleation stage, it reaches a plateau value after nucleation, and then decreases. The decrease is clearly observed for low and medium temperatures, and it is due to the merger of small-sized clusters into the large-sized clusters. In the meantime, at the nucleation point, N_L also starts to increase. It can be seen that N_L exhibits a maximum and then decreases as well due to merging of large-sized clusters with each other. It is important to note that at high temperatures despite the existence of clusters, strain hardening could not be observed at all within 200% elongation.

This is also depicted in the snapshots of the iPP during FIC at 370 K at different strains in Figure 5. Specifically, during the pre-nucleation stage at ϵ = 0.2 (Figure 6a), there are a few sparse small-sized clusters depicted in light blue and at the nucleation point (Figure 6b), large-sized clusters appear for the first time, depicted in red. At higher strains (Figure 6c), the small-sized clusters start to be depleted, and the large-sized clusters also merge with each other. Finally, at strains around 200%, a percolated network of clusters has been formed which has the structure of a shish morphology. All the clusters are oriented along the tensile direction. Following Dargazany et al.,[60] we have assumed that the semicrystalline samples created in this work are in the stage of the fibrillar crystal formation.

https://doi.org/10.1021/acs.macromol.3c00916
Macromolecules 2023, 56, 8417−8427

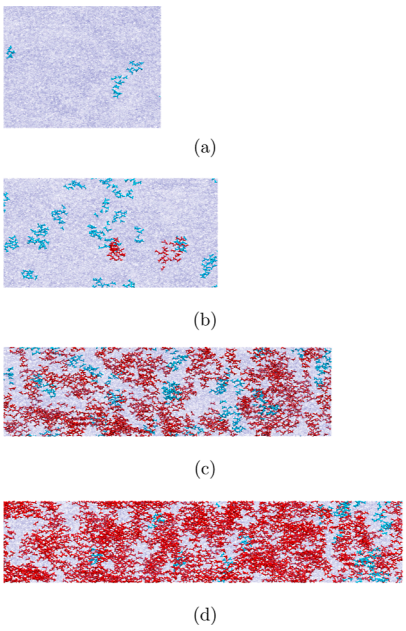

Figure 6. Snapshots of the iPP deformed box during FIC at 370 K (a) ϵ = 0.3, (b) ϵ = 0.7 (nucleation point), (c) ϵ = 1.5, and (d) ϵ = 2. In each snapshot, the large-sized clusters (red), the small-sized clusters (light blue), and the amorphous phase (ice-blue) are depicted.

3.5. Preordering. The local orientational order parameter $P_{2,i(\text{local})}$ for two groups of atoms, "nucleating" and "melting", along the $i \in \{x, y, z\}$ axis was quantified as described in Section 2. The classification time at 370 K, i.e., the time at which we classify the atoms in two groups, was chosen as 85 ns. The sensitivity of the analysis on the classification time is presented in the Supporting Information. In Figure 7a, the difference of the local orientational order parameter between these two groups $\Delta(P_{2,i(\text{local})})$ along $i \in \{x, y, z\}$ is depicted for a single simulation in the $N\dot{e}_{xx}P_{yy}P_{zz}T$ ensemble at 370 K. It can be seen that $P_{2,x(\text{local})}$ increases during the pre-nucleation stage. This reveals that the nucleating atoms have a higher ordering along the tensile axis (x axis) than do the melting atoms prior to nucleation. On the contrary, melting atoms are more aligned along the y and z direction. Moreover, the difference of the velocity $\Delta(u_i)$ between the "nucleating" and "melting" atoms along the $i = x$, y and z axis is plotted in Figure 7b. The velocity for each group was calculated as an average over all of the "nucleating" and "melting" atoms every 5 ns, respectively. It can be seen that the difference of the velocity along the x axis $\Delta(u_x)$ acquires negative values after 25 ns, while $\Delta(u_y)$ and $\Delta(u_z)$ increase. This means that the "nucleating" atoms are less mobile along the tensile direction, and their mobility increases perpendicular to the tensile direction with respect to "melting" atoms.

Overall, it can be said that there are areas of increased ordering prior to nucleation. The mobility of the atoms within these areas is restricted along the tensile direction, and it increases in the transverse direction. It has been shown in a previous dynamic Monte Carlo study[61] for a polymer system upon cooling that ordered polymer segments are less mobile and move together in the same direction in a correlated fashion. Based on this, we can assume that the polymer segments in the ordered regions cooperatively rearrange themselves along the transverse direction, in which direction they align parallel to each other and in the end crystallize. We also tried to calculate the Voronoi volume and compare the values for the two groups, but no clear trend could be extracted. On top of this, the exact sequence of conformation order, density fluctuation, and orientation order as it was described by Li et al.[22] could not be extracted. For the rest of the temperatures, $\Delta(P_{2,i(\text{local})})$ and $\Delta(u_i)$ exhibit similar behavior as at 370 K.

3.6. Crystallization Rates. Finally, the overall crystallization rate was measured. To extract the crystallization rate, five simulations per temperature were performed from 320 to 420 K with step 10 K for 400 ns in the $N\dot{e}_{xx}P_{yy}P_{zz}T$ ensemble with strain rate $\dot{e}_{xx} = 10^7\ \text{s}^{-1}$, as it was described in Section 2. The time evolution of crystallinity χ_c for certain temperatures is plotted in Figure 8a up to the cavitation point. Crystallization rate is described by the half time of the crystallization process, meaning the time for half of the material to have transformed into crystals. Though, in the present study due to cavitation, none of the graphs seems to exceed the value of $\chi_c = 0.4$. Cavitation, which was inevitable due to the high strain rate $\dot{e}_{xx} = 10^7\ \text{s}^{-1}$, takes place later in time at higher temperatures in comparison with lower temperatures. Previous molecular-dynamics studies on polyethylene under tensile deformation[62] have shown that cavitation can be avoided by repeating melting/recrystallization events using a lower strain rate $\dot{e}_{xx} = 5 \times 10^6\ \text{s}^{-1}$. We also studied FIC of iPP under $\dot{e}_{xx} = 5 \times 10^6\ \text{s}^{-1}$, but the formation of cavities at low crystallinity values was inevitable (see Supporting Information). For this reason, the crystallization rate was estimated as the inverse of the simulation time $(t_{\chi_c=0.2})^{-1}$ at which χ_c needs to

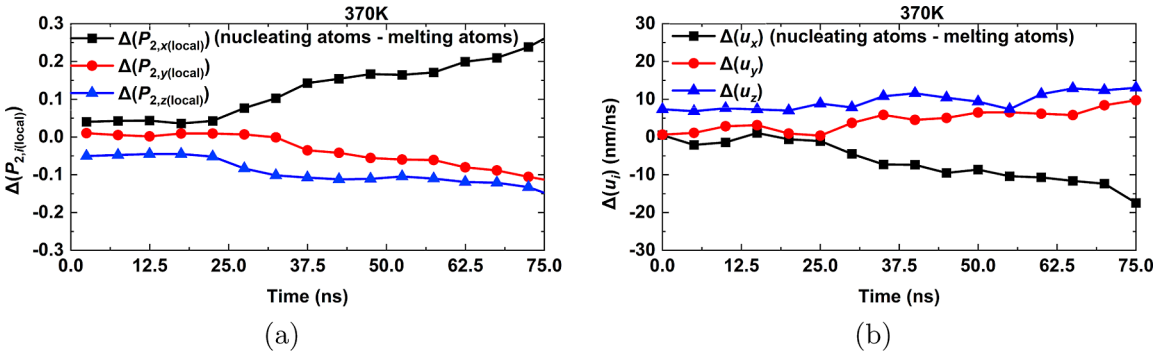

Figure 7. Time evolution of the difference of the (a) local orientational order parameter ($\Delta P_{2,i(\text{local})}$) and (b) velocity $\Delta(u_i)$ between "nucleating" and "melting" atoms along the x (black square), y (red circle), and z (blue triangle) direction. Both plots are extracted from a single simulation in the $N\dot{e}_{xx}P_{yy}P_{zz}T$ ensemble at 370 K with strain rate $10^7\ \text{s}^{-1}$. The differences are plotted up to nucleation point τ = 75 ns at 370 K, which was extracted using the MFPT method.

https://doi.org/10.1021/acs.macromol.3c00916
Macromolecules 2023, 56, 8417−8427

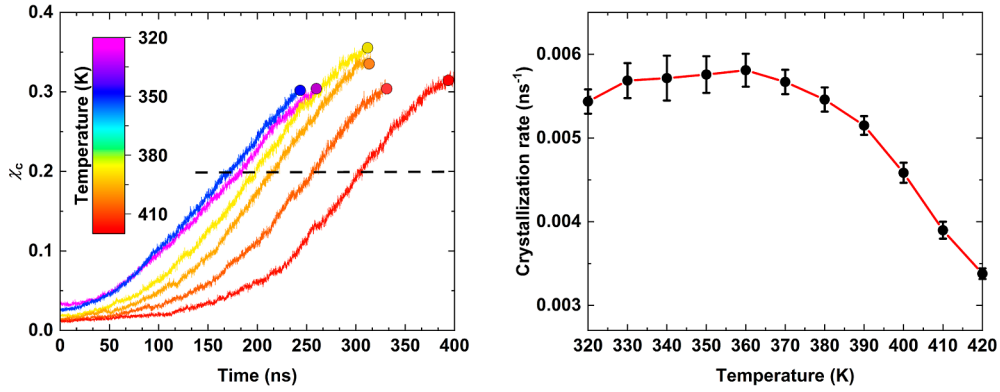

Figure 8. (a) Time evolution of crystallinity χ_c at different temperatures in the $N\dot{e}_{xx}P_{yy}P_{zz}T$ ensemble. The colored points signify the time at which the density decreased abruptly, indicating cavitation. The dashed line is drawn at χ_c equals 0.2. (b) Temperature dependence of the crystallization rate, which was estimated as the inverse of the simulation time $(t_{\chi_c=0.2})^{-1}$ at which χ_c equals 0.2. The error bars represent the standard deviation which was estimated from five simulations starting from a different initial sample at each temperature.

develop up to 0.2. The crystallization rate maximum lies in between 330−360 K and from 370 K onward, the curve starts decreasing (Figure 8b). Under quiescent conditions, Magill[52] has reported a maximum crystallization rate within 333−343 K, while Mubarak et al.[63] estimated the maximum crystallization rate at about 346 K.

The crystallinity measured prior to cavitation for the semicrystalline iPP samples produced at different temperatures, as was described, ranges from 0.30 to 0.36. Semicrystalline iPP cast films[64] and extruded sheets,[65] which were uniaxially drawn after their fabrication, exhibit crystallinity values ranging from 0.35 to 0.4 and from 0.25 to 0.6, respectively. Liu et al.[66] also reported for semicrystalline stretched iPP samples degrees of crystallinity varying from 0.25 to 0.4. It seems that the simulation results are consistent with the experimental values. However, in this study, flow is applied to supercooled melts, and there are only a few experimental studies that have reproduced a process like this. The difficulty lies on the fact that experimentally crystallization takes places before flow has any effect, e.g., in cast or blown films processing, a spherulitic structure has been created before any stretching. In 2010, Okada et al.[12] succeeded for the first time in realizing a strong melt elongation by developing a new compression method for iPP at 423 K. They reported that the nucleation rate increased drastically comparing to quiescent conditions and that crystals were formed at 1 ms, while the crystallization was completed at 4 ms—an MD simulation span the time scale of ns. The final crystallinity fraction was 0.92. In the current study, it would be rather difficult to reach such high crystallinity values taking into consideration the small time scale and the low stretch ratio compared to the aforementioned study. Lower stretch rates and longer annealing times can drastically enhance the degree of crystallinity. It should be noted that previous simulations studies reported crystallinity values for iPP equal to 0.25.[30]

3.7. Percolation of Cooperatively Rearranging Regions. Upon cooling, dynamic heterogeneity emerges, meaning that the polymer segments do not relax uniformly throughout the polymer bulk.[59] This was evident in the present study by measuring the reorientation relaxation time of Kuhn segments which increases drastically and exhibits a nonuniform behavior upon decreasing the temperature. The non-gaussian parameter was also found to be nonzero indicating that the united atoms are trapped in cages formed by their neighbors, which can vary in size. As predicted by the Adams-Gibbs theory,[67] dynamic heterogeneity is directly related to the variation of the size of the cooperatively rearranging regions (CRRs). Within CRRs, the movement of the polymer segments along certain directions is believed to be hindered,[61,67] as it was shown in the present study as well, if we suppose that the high ordering areas discussed in Section 3.5 identify with the CRRs. On top of this, due to this structural relaxation, the mechanical response of the segments within CRRs can be drastically affected. At low temperatures (350−370 K), where the crystallization rate maximum is observed, the dynamic heterogeneity is more prominent than at higher temperatures, meaning that the size of CRRs is larger.[67] A percolated network of CRRs in the supercooled state could possibly explain the strain hardening effect before nucleation (Figure 4a). At high temperatures (400−420 K), the size of CRRs is smaller and the dynamic relaxation of the local segments is significantly faster, explaining the negligible stress values despite the presence of nuclei.

4. CONCLUSIONS

We have performed molecular-dynamics simulations to study the FIC of iPP in a wide temperature range below the melting temperature of the isotropic melt T_m = 460 K[40] and above the estimated glass-transition temperature T_g = 305.6 K. It has been shown that iPP crystallizes within a few ns using a strain rate $\dot{\epsilon}$ equal to 10^7 s^{-1} and the temperature T_{max} at which the crystallization exhibits a maximum was found in the range of 330−360 K, in good agreement with experimental results for quiescent conditions. In the vicinity of T_{max}, a strain hardening was observed prior to nucleation, which coincides with the increase in the relaxation time of Kuhn segments as temperature decreases. Relaxation of Kuhn segments can be slowed down with decreasing the temperature due to increased cooperativity. Additionally, during the pre-nucleation stage, areas of high ordering were spotted. Within these areas, polymer segments move preferably perpendicular to the tensile direction in order to reorient themselves and, at the end, crystallize by forming a shish structure.

An immediate objective for future work is a deeper understanding of the high ordering areas during the pre-nucleation stage. In essence, are these high ordering areas

https://doi.org/10.1021/acs.macromol.3c00916
Macromolecules 2023, 56, 8417−8427

connected to the CRRs predicted by the Adams-Gibbs theory?[67] What is the topology of the CRRs and can the topology explain the maximum in the crystallization rate? On top of that, a study of the effect of strain rate on T_{max} would be of great importance.

■ ASSOCIATED CONTENT

Supporting Information

The Supporting Information is available free of charge at https://pubs.acs.org/doi/10.1021/acs.macromol.3c00916.

Additional simulation results on glass transition, segmental relaxation, pre-nucleation, and cavitation (PDF)

■ AUTHOR INFORMATION

Corresponding Author

Nikolaos I. Sigalas − *Soft Matter and Biological Physics Group, Department of Applied Physics, Technische Universiteit Eindhoven, 5600 MB Eindhoven, The Netherlands; DPI, 5600 AX Eindhoven, The Netherlands;* orcid.org/0000-0002-5184-433X; Email: n.sigalas@tue.nl

Authors

Stan A. T. Van Kraaij − *Soft Matter and Biological Physics Group, Department of Applied Physics, Technische Universiteit Eindhoven, 5600 MB Eindhoven, The Netherlands*

Alexey V. Lyulin − *Soft Matter and Biological Physics Group, Department of Applied Physics, Technische Universiteit Eindhoven, 5600 MB Eindhoven, The Netherlands; Center for Computational Energy Research (CCER), 5600 MB Eindhoven, The Netherlands;* orcid.org/0000-0002-7533-3366

Complete contact information is available at: https://pubs.acs.org/10.1021/acs.macromol.3c00916

Notes

The authors declare no competing financial interest.

■ ACKNOWLEDGMENTS

This research forms part of the research programme of DPI, project 831, and we thank the DPI industrial partners for the helpful discussions. This work was carried out on the Dutch national e-infrastructure with the support of SURF Cooperative. Additionally, we want to acknowledge the help and the great scientific support of Prof. Doros N. Theodorou and Dr. Stefanos D. Anogiannakis. We are also thankful to Prof. Gregory Rutledge and Dr. Marat Andreev for their insightful discussions on crystallization. Finally, we are grateful to MSc. Vincent E. Debets for sharing his knowledge on the glassy dynamics.

■ REFERENCES

(1) Lodge, T. P. Celebrating 50 Years of Macromolecules. *Macromolecules* **2017**, *50*, 9525−9527.

(2) Ebnesajjad, S. *Plastic Films in Food Packaging: Materials, Technology and Applications*, 1st ed.; Elsevier: Amsterdam, The Netherlands, 2013.

(3) Bauer, A.-S.; Tacker, M.; Uysal-Unalan, I.; Cruz, R. M. S.; Varzakas, T.; Krauter, V. Recyclability and redesign challenges in multilayer flexible food packaging—a review. *Foods* **2021**, *10*, 2702.

(4) Kaiser, K.; Schmid, M.; Schlummer, M. Recycling of polymer-based multilayer packaging: A review. *Recycling* **2018**, *3*, 1.

(5) Pettersen, M. K.; Grøvlen, M. S.; Evje, N.; Radusin, T. Recyclable mono materials for packaging of fresh chicken fillets: New design for recycling in circular economy. *Packag. Technol. Sci.* **2020**, *33*, 485−498.

(6) Guerritore, M.; Olivieri, F.; Castaldo, R.; Avolio, R.; Cocca, M.; Errico, M. E.; Galdi, M. R.; Carfagna, C.; Gentile, G. Recyclable-by-design mono-material flexible packaging with high barrier properties realized through graphene hybrid coatings. *Resour., Conserv. Recycl.* **2022**, *179*, 106126.

(7) *Borstar-Based Full PE Laminate Solution Improves Recyclability of Flexible Packaging Materials—Borealis*, 2016. https://www.borealisgroup.com (accessed Feb 07, 2023).

(8) Chen, W.; Zhang, Q.; Zhao, J.; Li, L. Molecular and thermodynamics descriptions of flow-induced crystallization in semi-crystalline polymers. *J. Appl. Phys.* **2020**, *127*, 127.

(9) Chatterjee, T.; Patel, R.; Garnett, J.; Paradkar, R.; Ge, S.; Liu, L.; Forziati, K. T.; Shah, N. Machine direction orientation of high density polyethylene (HDPE): Barrier and optical properties. *Polymer* **2014**, *55*, 4102−4115.

(10) Hatfield, E. *Multilayer Flexible Packaging*, 2nd ed.; Wagner, J. R., Ed.; *Plastics Design Library*; William Andrew Publishing, 2016; pp 147−152.

(11) Ji, H.; Zhou, X.; Chen, X.; Zhao, H.; Wang, Y.; Zhu, H.; Ma, Y.; Xie, L. Deformation-induced crystallization behavior of isotactic polypropylene sheets containing a β-nucleating agent under solid-state stretching. *Polymers* **2020**, *12*, 1258.

(12) Okada, K. N.; Washiyama, J.; Watanabe, K.; Sasaki, S.; Masunaga, H.; Hikosaka, M. Elongational crystallization of isotactic polypropylene forms nano-oriented crystals with ultra-high performance. *Polym. J.* **2010**, *42*, 464−473.

(13) Gloger, D.; Rossegger, E.; Gahleitner, M.; Wagner, C. Plastic drawing response in the biaxially oriented polypropylene (BOPP) process: polymer structure and film casting effects. *J. Polym. Eng.* **2020**, *40*, 743−752.

(14) Sadeghi, F.; Tabatabaei, S. H.; Ajji, A.; Carreau, P. J. Properties of uniaxially stretched polypropylene films: Effect of drawing temperature and random copolymer content. *Can. J. Chem. Eng.* **2010**, *88*, 1091−1098.

(15) Deng, B.; Chen, L.; Zhong, Y.; Li, X.; Wang, Z. The effect of temperature on the structural evolution of ultra-high molecular weight polyethylene films with pre-reserved shish crystals during the stretching process. *Polymer* **2023**, *267*, 125690.

(16) Okada, K. N.; Tagashira, K.; Sakai, K.; Masunaga, H.; Hikosaka, M. Temperature dependence of crystallization of nano-oriented crystals of iPP and the formation mechanism. *Polym. J.* **2013**, *45*, 70−78.

(17) Nie, C.; Peng, F.; Cao, R.; Cui, K.; Sheng, J.; Chen, W.; Li, L. Recent progress in flow-induced polymer crystallization. *J. Polym. Sci.* **2022**, *60*, 3149−3175.

(18) Olmsted, P. D.; Poon, W. C. K.; Mcleish, T. C. B.; Terrill, N. J.; Ryan, A. J. Spinodal-Assisted Crystallization in Polymer Melts. *Phys. Rev. Lett.* **1998**, *81*, 373−376.

(19) Terrill, N. J.; Fairclough, P. A.; Towns-Andrews, E.; Komanschek, B. U.; Young, R. J.; Ryan, A. J. Density fluctuations: The nucleation event in isotactic polypropylene crystallization. *Polymer* **1998**, *39*, 2381−2385.

(20) Strobl, G. From the melt via mesomorphic and granular crystalline layers to lamellar crystallites: A major route followed in polymer crystallization? *Eur. Phys. J. E* **2000**, *3*, 165−183.

(21) Wurm, A.; Soliman, R.; Goossens, J. G.; Bras, W.; Schick, C. Evidence of pre-crystalline-order in super-cooled polymer melts revealed from simultaneous dielectric spectroscopy and SAXS. *J. Non-Cryst. Solids* **2005**, *351*, 2773−2779.

(22) Su, F.; Ji, Y.; Meng, L.; Wang, Z.; Qi, Z.; Chang, J.; Ju, J.; Li, L. Coupling of Multiscale Orderings during Flow-Induced Crystallization of Isotactic Polypropylene. *Macromolecules* **2017**, *50*, 1991−1997.

(23) Anwar, M.; Berryman, J. T.; Schilling, T. Crystal nucleation mechanism in melts of short polymer chains under quiescent conditions and under shear flow. *J. Chem. Phys.* **2014**, *141*, 124910.

(24) An, H.; Zhao, B.; Ma, Z.; Shao, C.; Wang, X.; Fang, Y.; Li, L.; Li, Z. Shear-Induced Conformational Ordering in the Melt of Isotactic Polypropylene. *Macromolecules* **2007**, *40*, 4740−4743.

(25) An, H.; Li, X.; Geng, Y.; Wang, Y.; Wang, X.; Li, L.; Li, Z.; Yang, C. Shear-induced conformational ordering, relaxation, and crystal-

lization of isotactic polypropylene. *J. Phys. Chem. B* **2008**, *112*, 12256−12262.
(26) Wedekind, J.; Strey, R.; Reguera, D. New method to analyze simulations of activated processes. *J. Chem. Phys.* **2007**, *126*, 134103.
(27) Yi, P.; Rutledge, G. C. Molecular simulation of bundle-like crystal nucleation from n-eicosane melts. *J. Chem. Phys.* **2011**, *135*, 024903.
(28) Nicholson, D. A.; Rutledge, G. C. Molecular simulation of flow-enhanced nucleation in n-eicosane melts under steady shear and uniaxial extension. *J. Chem. Phys.* **2016**, *145*, 244903.
(29) Yi, P.; Locker, C. R.; Rutledge, G. C. Molecular dynamics simulation of homogeneous crystal nucleation in polyethylene. *Macromolecules* **2013**, *46*, 4723−4733.
(30) Yamamoto, T. Molecular Dynamics of Crystallization in a Helical Polymer Isotactic Polypropylene from the Oriented Amorphous State. *Macromolecules* **2014**, *47*, 3192−3202.
(31) Martin, M. G.; Siepmann, J. I. Novel Configurational-Bias Monte Carlo Method for Branched Molecules. Transferable Potentials for Phase Equilibria. 2. United-Atom Description of Branched Alkanes. *J. Phys. Chem. B.* **1999**, *103*, 4508−4517.
(32) Pütz, M.; Curro, J. G.; Grest, G. S. Self-consistent integral equation theory for polyolefins: Comparison to molecular dynamics simulations and X-ray scattering. *J. Chem. Phys.* **2001**, *114*, 2847−2860.
(33) Kuppa, V. K.; In't Veld, P. J.; Rutledge, G. C. Monte Carlo simulation of interlamellar isotactic polypropylene. *Macromolecules* **2007**, *40*, 5187−5195.
(34) Romanos, N.; Megariotis, G.; Theodorou, D. N. Molecular dynamics simulations of stretch-induced crystallization in layered polyethylene. *Polym. Cryst.* **2021**, *4*, No. e210172.
(35) Ranganathan, R.; Kumar, V.; Brayton, A. L.; Kröger, M.; Rutledge, G. C. Atomistic Modeling of Plastic Deformation in Semicrystalline Polyethylene: Role of Interphase Topology, Entanglements, and Chain Dynamics. *Macromolecules* **2020**, *53*, 4605−4617.
(36) Paul, W.; Yoon, Y.; Smith, G. D. An optimized united atom model for simulations of polymethylene melts. *J. Chem. Phys.* **1995**, *103*, 1702−1709.
(37) Ramos, J.; Vega, J. F.; Martínez-Salazar, J. Molecular Dynamics Simulations for the Description of Experimental Molecular Conformation, Melt Dynamics, and Phase Transitions in Polyethylene. *Macromolecules* **2015**, *48*, 5016−5027.
(38) Van Der Spoel, D.; Lindahl, E.; Hess, B.; Groenhof, G.; Mark, A. E.; Berendsen, H. J. C. GROMACS: Fast, flexible, and free. *J. Comput. Chem.* **2005**, *26*, 1701−1718.
(39) Theodorou, D. N.; Suter, U. W. Detailed molecular structure of a vinyl polymer glass. *Macromolecules* **1985**, *18*, 1467−1478.
(40) Yamada, K.; Hikosaka, M.; Toda, A.; Yamazaki, S.; Tagashira, K. Equilibrium melting temperature of isotactic polypropylene with high tacticity: 1. Determination by differential scanning calorimetry. *Macromolecules* **2003**, *36*, 4790−4801.
(41) Parrinello, M.; Rahman, A. Polymorphic transitions in single crystals: A new molecular dynamics method. *J. Appl. Phys.* **1981**, *52*, 7182−7190.
(42) Sigalas, N. I.; Anogiannakis, S. D.; Theodorou, D. N.; Lyulin, A. V. A coarse-grained model for capturing the helical behavior of isotactic polypropylene. *Soft Matter* **2022**, *18*, 3076−3086.
(43) Moss, G. P. Basic terminology of stereochemistry (IUPAC Recommendations 1996). *Pure Appl. Chem.* **1996**, *68*, 2193−2222.
(44) Chkonia, G.; Wölk, J.; Strey, R.; Wedekind, J.; Reguera, D. Evaluating nucleation rates in direct simulations. *J. Chem. Phys.* **2009**, *130*, 064505.
(45) Anwar, M.; Graham, R. S. Molecular dynamics simulations of crystal nucleation in entangled polymer melts under start-up shear conditions. *J. Chem. Phys.* **2019**, *150*, 084905.
(46) Fetters, L. J.; Lohse, D. J.; García-Franco, C. A.; Brant, P.; Richter, D. Prediction of Melt State Poly(α-olefin) Rheological Properties: The Unsuspected Role of the Average Molecular Weight per Backbone Bond. *Macromolecules* **2002**, *35*, 10096−10101.
(47) Tzoumanekas, C.; Theodorou, D. N. Topological analysis of linear polymer melts: A statistical approach. *Macromolecules* **2006**, *39*, 4592−4604.
(48) Eckstein, A.; Suhm, J.; Friedrich, C.; Maier, R. D.; Sassmannshausen, J.; Bochmann, M.; Mülhaupt, R. Determination of plateau moduli and entanglement molecular weights of isotactic, syndiotactic, and atactic polypropylenes synthesized with metallocene catalysts. *Macromolecules* **1998**, *31*, 1335−1340.
(49) Freischmidt, H. M.; Shanks, R. A.; Moad, G.; Uhlherr, A. Characterization of polyolefin melts using the polymer reference interaction site model integral equation theory with a single-site united atom model. *J. Polym. Sci., Part B: Polym. Phys.* **2001**, *39*, 1803−1814.
(50) Cowie, J. M. Glass transition temperatures of stereoblock, isotactic and atactic polypropylenes of various chain lengths. *Eur. Polym. J.* **1973**, *9*, 1041−1049.
(51) De Rosa, C.; Scoti, M.; Di Girolamo, R.; Ballesteros, O. R.; Auriemma, F.; Malafronte, A. Polymorphism in polymers: A tool to tailor material's properties. *Polym. Cryst.* **2020**, *3*, No. e10101.
(52) Magill, J. H. A new technique for following rapid rates of crystallization II Isotactic polypropylene. *Polymer* **1962**, *3*, 35−42.
(53) Okui, N.; Umemoto, S.; Kawano, R.; Mamun, A. *Progress in Understanding of Polymer Crystallization*; Springer Berlin Heidelberg: Berlin, Heidelberg, 2007; pp 391−425.
(54) Waheed, N.; Ko, M. J.; Rutledge, G. C. *Progress in Understanding of Polymer Crystallization*; Springer Berlin Heidelberg: Berlin, Heidelberg, 2007; pp 457−480.
(55) Pals, D. T. F.; Van Der Zee, P.; Albers, J. H. M. Influence of stretching on the fusion behavior of stress-crystallized polypropylene films. *J. Macromol. Sci., Phys. B* **1972**, *6*, 739−759.
(56) Batistakis, C.; Lyulin, A. V.; Michels, M. A. J. Slowing down versus acceleration in the dynamics of confined polymer films. *Macromolecules* **2012**, *45*, 7282−7292.
(57) Vorselaars, B.; Lyulin, A. V.; Karatasos, K.; Michels, M. A. J. Non-Gaussian nature of glassy dynamics by cage to cage motion. *Phys. Rev. E: Stat., Nonlinear, Soft Matter Phys.* **2007**, *75*, 011504.
(58) Weeks, E. R.; Crocker, J. C.; Levitt, A. C.; Schofield, A.; Weitz, D. A. Three-Dimensional Direct Imaging of Structural Relaxation Near the Colloidal Glass Transition. *Science* **2000**, *287*, 627−631.
(59) Janssen, L. M. C. Mode-Coupling Theory of the Glass Transition: A Primer. *Front. Physiol.* **2018**, *6*, 97.
(60) Dargazany, R.; Khiêm, V. N.; Poshtan, E. A.; Itskov, M. Constitutive modeling of strain-induced crystallization in filled rubbers. *Phys. Rev. E: Stat., Nonlinear, Soft Matter Phys.* **2014**, *89*, 022604.
(61) Nie, Y.; Ye, X.; Zhou, Z.; Hao, T.; Yang, W.; Lu, H. Structural characteristics of a cooperatively rearranging region during the glass transition of a polymer system. *RSC Adv.* **2015**, *5*, 17726−17731.
(62) Yeh, I.-C.; Andzelm, J. W.; Rutledge, G. C. Mechanical and Structural Characterization of Semicrystalline Polyethylene under Tensile Deformation by Molecular Dynamics Simulations. *Macromolecules* **2015**, *48*, 4228−4239.
(63) Mubarak, Y.; Harkin-Jones, E. M.; Martin, P. J.; Ahmad, M. Modeling of non-isothermal crystallization kinetics of isotactic polypropylene. *Polymer* **2001**, *42*, 3171−3182.
(64) Chen, X.; Lv, F.; Su, F.; Ji, Y.; Meng, L.; Wan, C.; Lin, Y.; Li, X.; Li, L. Deformation mechanism of iPP under uniaxial stretching over a wide temperature range: An in-situ synchrotron radiation SAXS/WAXS study. *Polymer* **2017**, *118*, 12−21.
(65) Bao, R.; Ding, Z.; Zhong, G.; Yang, W.; Xie, B.; Yang, M. Deformation-induced morphology evolution during uniaxial stretching of isotactic polypropylene: Effect of temperature. *Colloid Polym. Sci.* **2012**, *290*, 261−274.
(66) Liu, X.; Zou, L.; Chang, B.; Shi, H.; Yang, Q.; Cheng, K.; Li, T.; Schneider, K.; Heinrich, G.; Liu, C.; Shen, C. Strain dependent crystallization of isotactic polypropylene during solid-state stretching. *Polym. Test.* **2021**, *104*, 107404.
(67) Adam, G.; Gibbs, J. H. On the temperature dependence of cooperative relaxation properties in glass-forming liquids. *J. Chem. Phys.* **1965**, *43*, 139−146.

https://doi.org/10.1021/acs.macromol.3c00916
Macromolecules 2023, 56, 8417−8427